ELSEVIER

Contents lists available at ScienceDirect

Journal of Electroanalytical Chemistry

journal homepage: www.elsevier.com/locate/jelechem



Ru-CoO heterostructured nanoparticles supported on nitrogen and sulfur codoped graphene nanosheets as effective electrocatalysts for hydrogen evolution reaction in alkaline media



Warisha Naseeb a,b, Qiming Liu b, Forrest Nichols b, Dingjie Pan b, Muhammad Kaleem Khosa a,*, Shaowei Chen b,*

ARTICLE INFO

Keywords: Sulfur,nitrogen-codoped graphene Ruthenium Cobalt oxide Heterostructure Hydrogen evolution reaction

ABSTRACT

Production of clean hydrogen energy from water splitting is vital for the future fuel industry, and nanocomposites have emerged as effective catalysts for the hydrogen evolution reaction (HER). In this study, Ru-CoO@SNG nanocomposites are prepared by controlled pyrolysis where Ru-CoO heterostructured nanoparticles are supported on nitrogen and sulfur codoped graphene oxide nanosheets. With a large surface area, the obtained composites exhibit a remarkable electrocatalytic activity toward HER in 1.0 M KOH with an overpotential of only $-90~\rm mV$ to reach the current density of 10 mA cm $^{-2}$, in comparison to $-60~\rm mV$ for commercial Pt/C benchmark, along with high stability. Mechanistically, codoping of sulfur and nitrogen facilitates the dispersion of the nanoparticles, and the formation of Ru-CoO heterostructures increases the active site density, reduces the electron-transfer kinetics and boosts the catalytic performance. Results from this study highlight the unique potential of structural engineering in enhancing the electrocatalytic performance of heterostructured nanocomposites.

1. Introduction

Hydrogen has been considered as one of the most promising energy sources in the future owing to its clean and environmentally friendly nature [1-3]. Within this context, it is vital to develop effective and sustainable technologies for hydrogen production, storage and conversion [4-6]. Water electrolysis through electrochemical hydrogen evolution reaction (HER) has emerged as a viable technology [7-10], where the performance is dictated largely by the electrode catalysts [11-13]. Currently, Pt-based materials are used as the benchmark electrocatalysts, but the limited natural abundance and high cost of Pt has significantly hindered its large-scale commercialization [14,15]. Furthermore, the performance may diminish due to aggregation of Pt and corrosion of the carbon scaffold during prolonged operation [16]. Thus, there is an urgent need to design non-Pt, highly stable and low-cost electrocatalysts for HER [17-20]. Among these, ruthenium (Ru) is a favorable alternative to Pt due to its reduced cost (only a fraction of that for Pt), and hydrogen adsorption strength of 65 kcal mol⁻¹ that is similar to that of Pt [21,22]. Moreover, Ru has shown stability in both acidic and alkaline media and is more adaptable to a versatile range of working conditions, in comparison to Pt which exhibits only limited long-term stability in basic environment [23,24]. All these factors have weighed in to boost the development of Ru-based HER catalysts in recent years [25]. Generally, water electrolysis at room temperature can be performed in both acidic and alkaline electrolytes. Yet the activity of Pt in alkaline media is two to three orders of magnitude lower than in acidic solutions, because the HER kinetics is hindered by the limited hydrogen ion (H⁺) concentration in alkaline media resulting in high overpotentials [26–29]. In fact, the initial water dissociation step that generates protons for the subsequent reactions results in the lethargic reaction rate of HER in alkaline media [30,31]. Therefore, the search for effective electrocatalysts to overcome the energetic barrier and enhance the reaction kinetics in alkaline electrolytes has been attracting extensive attraction [32].

Towards this end, extensive research has been devoted to the rational design and engineering of transition metal-oxide based nanocomposites [33,34], where the active sites can be enriched by doping with select heteroatoms [35–38] to facilitate good dispersion of the metal species and hinder their agglomeration [39]. Notably, the electrocatalytic performance may be enhanced by the formation of heterostructures [40,41], due to interfacial charge transfer and manipulation of the valence state [42,43]. For instance, Wang et al.

E-mail addresses: mkhosapk@yahoo.com (M.K. Khosa), shaowei@ucsc.edu (S. Chen).

^a Department of Chemistry, Government College University, Faisalabad, Pakistan

^bDepartment of Chemistry and Biochemistry, University of California, 1156 High Street, Santa Cruz, CA 95064, United States

^{*} Corresponding authors.

[44] prepared Ru-NiWN_x heterostructures by coupling ruthenium with hybrid metal nitrides (a mixture of tungsten nitride and nickel nitride) through a simple nitridation route. The heterogenous interface resulted in abundance of catalytic active sites and strong electronic interactions between ruthenium and the supporting matrix, delivering a low overpotential (η_{100}) of -70 mV to reach the current density of 100 mA cm⁻² in alkaline media. Hoa et al. [45] synthesized Ru-MoS₂-Mo₂C heterostructures over TiN nanorod arrays supported on carbon cloth through a hydrothermal and carburization treatment and achieved a low cell voltage of 1.49 V at 10 mA cm⁻² in 1 M KOH for full water splitting, owing to the high charge-transfer ability and large electrochemically active surface area of the heterostructured catalysts. Sun et al. [46] reported the formation of a heterojunction interface by coupling nickel-iron layered double hydroxide and ruthenium oxide on T-shaped NiTe via a hydrothermal procedure. The obtained NiTe@RuO₂/NF catalyst delivered an ultralow overpotential (η₁₀) of -19 mV at 10 mA cm⁻² in 1 M KOH. The high activity was due to electron transfer from RuO2 to NiTe that modulated the HER reaction pathway. Geng et al. [47] embedded Ni/MoC heteronanoparticles into nitrogen-doped carbon nanotube arrays on carbon cloth by alkaline etching followed by pyrolysis, and observed a low η_{10} of -70 mV in 1 M KOH, due to electron transfer between Ni and MoC and the binder-free electrode configuration.

Herein we report the pyrolytic synthesis of nanocomposites with Ru-CoO heterostructured nanoparticles embedded within S and N codoped graphene oxide nanosheets (Ru-CoO@SNG). The obtained Ru-CoO@SNG nanocomposites exhibited a remarkable HER activity in alkaline media, with an η_{10} of -90 mV and a Tafel slope of 77 mV dec $^{-1}$. Such a performance was markedly higher than those of the metal-free SNG, Ru@SNG and CoO@SNG, and only slightly subpar as compared to that of commercial Pt/C ($\eta_{10}=$ -60 mV), suggesting that the electrocatalytic activity was most likely due to the synergistic interactions between Ru and CoO within the heterostructures.

2. Experimental section

2.1. Chemicals

Graphite powders (Spectrum Chemicals), sodium nitrate (NaNO $_3$, 99 %, Acros), sulfuric acid (H $_2$ SO $_4$, 98 %, Fisher Scientific), potassium permanganate (KMnO $_4$, 99 %, Fisher Scientific), hydrogen peroxide (H $_2$ O $_2$, 30 %, Fisher Scientific), hydrochloric acid (HCl, 37 %, Fisher Scientific), thiourea (99 %, Acros), ruthenium(III) chloride (RuCl $_3$, 35–40 % Ru, Acros), cobalt(II) chloride (CoCl $_2$, 98 %, Fisher Scientific), and potassium hydroxide (KOH, Fisher Scientific) were all used as received. Water was supplied by a Barnstead Nanopure water system (18.3 M Ω cm).

2.2. Sample preparation

Graphene oxide (GO) was synthesized by a modified Hummers method [48]. In a typical experiment, graphite flakes (1 g) were transferred into a 250 mL round-bottom flask. 23 mL of concentrated $\rm H_2SO_4$ was added into the flask and the mixture was stirred at room temperature for 24 h before being heated in an oil bath at 40 °C. 100 mg of NaNO₃ was added to the suspension and allowed to dissolve in 5 min followed by the slow addition of 3 g of KMnO₄ under magnetic stirring for 30 min, with the solution temperature kept below 45 °C. The flask was removed from the oil bath and 140 mL of Nanopure water and 10 mL of 30 % $\rm H_2O_2$ were added to the reaction vessel under magnetic stirring at room temperature for 5 min. The mixture was then centrifuged and washed with a 5 % HCl solution twice, followed by rinsing with copious amounts of water. The final precipitate was dispersed in 100 mL of water under sonication for 30 min. Insoluble solids were removed by centrifugation at 3000 rpm for 5 min, and

the brown supernatant (GO nanosheets) was collected and dried in an oven at 70 $^{\circ}\text{C}.$

To prepare S,N-codoped GO, 60 mg of GO, 120 mg of thiourea, and 30 mL of $\rm H_2O$ were added into a 100 mL flask and mixed under sonication overnight before being loaded into a Teflon-lined autoclave for hydrothermal treatment at 180 °C for 12 h, affording S,N-codoped GO which was denoted as SNGO.

To synthesize Ru-CoO@SNG, the SNGO dispersion obtained above was transferred to a flask, into which were added 0.065 mmol of RuCl₃·xH₂O and 0.016 mmol of CoCl₂·6H₂O The flask was then heated in an oil bath at 90 °C for 4 h, and the precipitates were obtained by centrifugation at 6000 rpm for 5 min, rinsed with H₂O, and dried at 60 °C in a vacuum oven overnight before being heated at 700 °C for 3 h in a nitrogen atmosphere at the nitrogen flow rate of 150 mL min $^{-1}$. The resulting sample was denoted as Ru-CoO@SNG.

Three control samples were synthesized at the same mass feeds, one without the addition of $CoCl_2$, a second without $RuCl_3$, and a third without any metal salts. They were referred to as Ru@SNG, CoO@SNG, and SNG, respectively.

2.3. Characterizations

Transmission electron microscopy (TEM) measurements were carried out on a JOEL JEM 2100F microscope equipped with an Oxford instruments energy dispersive X-ray spectroscopy (EDS) attachment. X-ray diffraction (XRD) patterns were acquired with a Rigaku Smartlab Diffractometer with Cu K_{α} radiation ($\lambda=1.5406~\mbox{Å})$, where the samples were deposited onto an aluminum plate and the measurements were conducted at a scan rate of 3° min $^{-1}$ and a step size of 0.02°. X-ray photoelectron spectroscopy (XPS) measurements were performed with a Phi 5400/XPS instrument equipped with an Al K_{α} source operated at 350 W and 10^{-9} torr, where the binding energies were calibrated against that of the C 1s electrons.

2.4. Electrochemistry

Electrochemical measurements were performed with a CHI 710 electrochemical workstation, and electrochemical impedance measurements were carried out with a Gamry Reference 600 instrument. A glassy carbon electrode (surface area 0.196 cm⁻²) was used as the working electrode, while a Ag/AgCl (1.0 M KCl) electrode and a graphite rod were used as the reference and counter electrodes, respectively. The Ag/AgCl electrode was calibrated against a reversible hydrogen electrode (RHE) and all potentials in the present study were referenced to this RHE, unless specified otherwise. To prepare the catalyst inks, 2 mg of the nanocomposites obtained above was sonicated for 10 min in isopropanol (1 mL), followed by the addition of Nafion (20 µL) binder (for good dispersion and layer integrity) and under sonication for an additional 20 min. 30 μL of the prepared inks was dropcast onto the surface of the glassy carbon electrode and dried at room temperature, corresponding to a catalyst mass loading of 0.244 mg cm⁻². Finally, 6 μL of Nafion (20 wt%) in isopropanol was added onto the prepared catalyst surface and allowed to dry, before the electrode was immersed into an electrolyte solution for data collection.

3. Results and discussion

3.1. Structural characterizations

The structure of the Ru-CoO@SNG nanocomposites was first characterized by TEM measurements. From the TEM images in Fig. 1a and S1, one can see that a number of high-contrast nanoparticles were produced and evenly distributed onto the low-contrast scaffold, falling in the size range of 2 to 8 nm (Fig. 1a inset) with an average size of

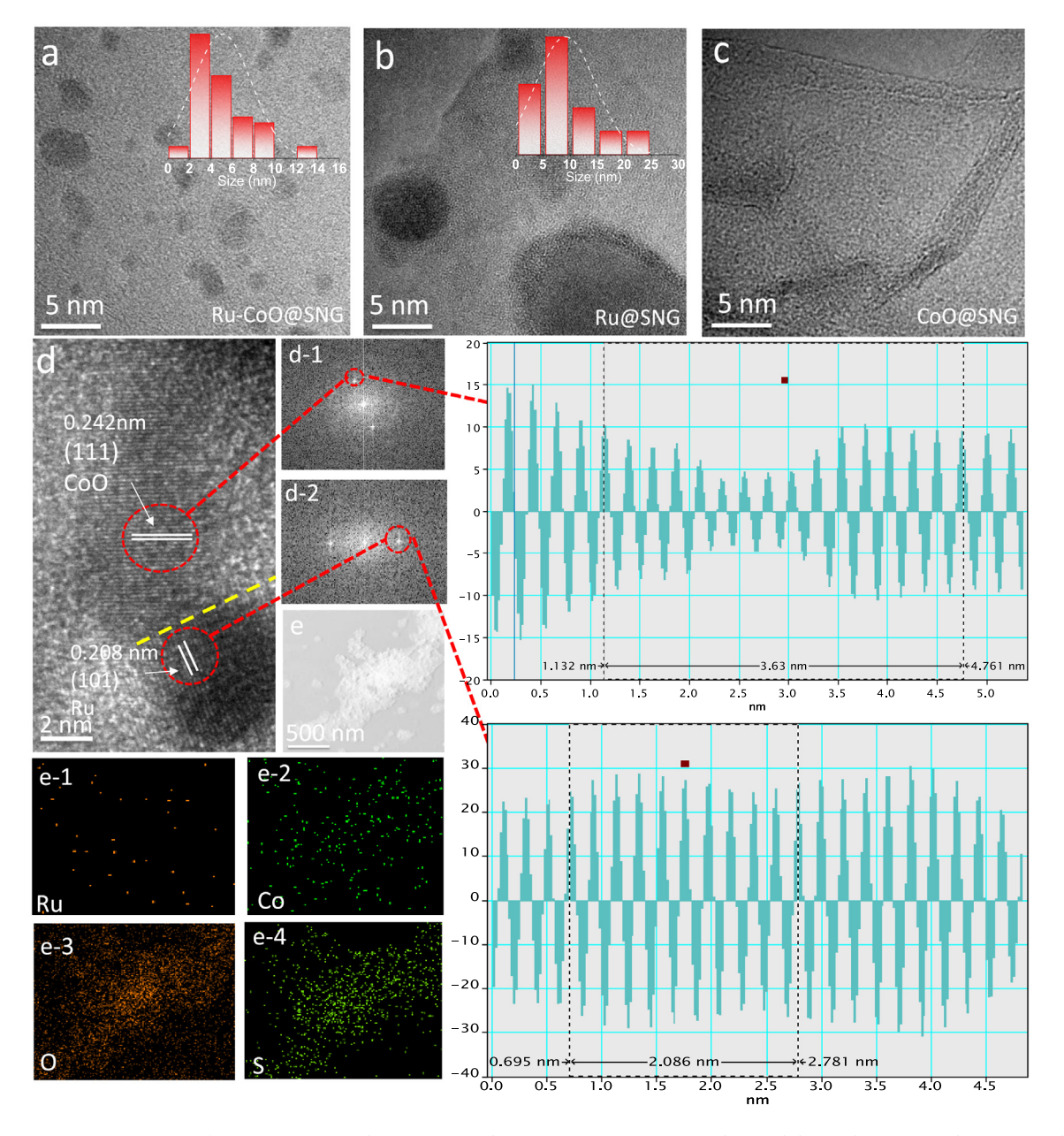


Fig. 1. Representative TEM images of (a) Ru-CoO@SNG, (b) Ru@SNG, and (c) CoO@SNG. Insets to panel (a) and (b) are the corresponding core size histograms. (d) HRTEM image of Ru-CoO@SNG featuring the corresponding lattice fringes of Ru and CoO with the corresponding FFT patterns in (d-1) and (d-2) of the red encircled areas and the live profiles of the interplanar distances of Ru(101) and CoO(111) lattice fringes by Gatan DigitalMicrograph. (e) HAADF-STEM image of Ru-CoO@SNG and the corresponding elemental maps of (e-1) Ru, (e-2) Co, (e-3) O, and (e-4) S.

5.0 ± 0.7 nm. In high-resolution TEM measurements (Fig. 1d and S2), the nanoparticles can be seen to display well-defined lattice fringes featuring two interplanar spacings of 0.208 and 0.242 nm that can be ascribed to the hexagonal Ru(101) (JCPDS card no. 65-7646) [49] and cubic CoO(111) planes (JCPDS card no. 78-0431) [50,51], respectively, as manifested in the live profiles. The corresponding FFT patterns are shown in Figs. 1d-1 and 1d-2. These two crystalline domains are in intimate contact, suggesting the formation of Ru-CoO heterostructures in the sample. In high-angle annular dark-field scanning TEM (HAADF-STEM) measurements (Fig. 1e), EDS-based elemental mapping analysis demonstrates that the Ru (Fig. 1e-1) and Co (Fig. 1e-2) elements were distributed rather evenly throughout the O (Fig. 1e-3) and S (Fig. 1e-4) decorated scaffold. The Ru@SNG sample also possessed a number of nanoparticles (Fig. 1b and S3), which were

significantly larger at 5 to 15 nm in diameter with an average size of 9.1 \pm 0.4 nm (Fig. 1b inset) and also displayed the Ru(101) lattice fringes, suggesting that Ru nanoparticles were indeed produced in the sample. By contrast, CoO@SNG (Fig. 1c and S4) displayed no nanoparticles, suggesting the formation of a mostly amorphous structure.

The XRD patterns are shown in Fig. 2a. All samples can be seen to exhibit a broad peak at $2\theta = 26.5^{\circ}$ that can be assigned to the graphene (002) facets (JCPDS card no. 65-6212) [52], suggesting successful reduction of graphene oxide to graphene during pyrolysis. Ru-CoO@SNG and Ru@SNG also showed a series of additional peaks at $2\theta = 38.2^{\circ}$, 43.3° , 44.4° , 64.8° and 77.9° that can be assigned to the (100), (002), (101), (102) and (103) facets of hexagonal Ru (JCPDS card no. 65-7646) [53], whereas no diffraction patterns of

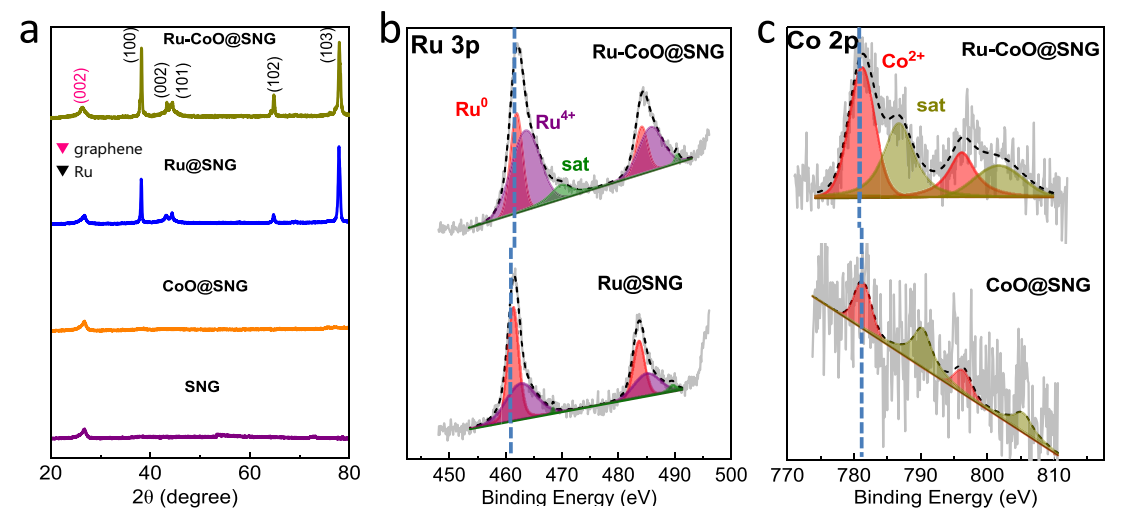


Fig. 2. (a) XRD patterns of Ru-CoO@SNG, Ru@SNG, CoO@SNG, and SNG. High-resolution XPS spectra of the (b) Ru 3p and (c) Co 2p electrons of Ru-CoO@SNG, Ru@SNG, CoO@SNG. Gray solid curves are experimental raw data and colored curves are deconvolution fits.

metallic cobalt or cobalt oxides could be detected with CoO@SNG, confirming the formation of an amorphous structure, as suggested in TEM measurements.

The elemental composition and valence states were then investigated by XPS measurements. Fig. S5a shows the survey spectra of the four samples, where the peaks at 164, 284, 399 and 531 eV can be assigned to the S 2p, C 1s, N 1s and O 1s electrons, respectively [54]. The Ru@SNG samples also contained the Ru 3p peaks at ca. 461 eV, and CoO@SNG possessed the Co 2p peaks at 781 eV, whereas both features can be found in Ru-CoO@SNG, consistent with their nanocomposite compositions. Furthermore, based on the integrated peak areas, the elemental composition of Ru-CoO@SNG was estimated to be 80.59 at% C, 2.26 at% N, 2.86 at% S, 12.46 at% O, 1.43 at% Ru and 0.37 at% Co; whereas the Ru and Co contents were found to be 0.89 at% and 0.13 at% for Ru@SNG and CoO@SNG, respectively (Table S1). The high-resolution XPS scans of the C 1s and Ru 3d electrons are shown in Fig. S5b. From the deconvolution of the spectra, one can see that all samples contained three species, 284.61 eV for sp2-hybridized C (C=C), 285.55 eV for sp3 C, and 289.33 eV for O-C=O [55,56]; and for Ru-CoO@SNG and Ru@SNG two additional doublets can be identified at 280.33/284.53 and 281.10/285.30 eV for the former and 280.09/284.29 and 280.97/285.17 eV for the latter, due to $3d_{5/2}/3d_{3/2}$ electrons of metallic Ru and Ru⁴⁺, respectively [57,58]. Consistent results were obtained in the Ru 3p scans (Fig. 2b), where Ru-CoO@SNG and Ru@SNG samples can be seen to consist of two doublets, 461.91/484.11 and 463.52/485.72 eV for the former and 461.42/483.62 and 462.90/485.10 eV for the latter [59-61]. The lower-energy pairs are due to metallic Ru whereas the high-energy pairs to Ru⁴⁺ species. One can see that the Ru binding energies of Ru-CoO@SNG was appreciably higher (by 0.2 eV for Ru 3d and 0.5 eV for Ru 3p) than those of Ru@SNG (Table S2), suggesting that Ru became electron-deficient in the Ru-CoO heterostructures, as compared to the

The Co 2p spectra of Ru-CoO@SNG and CoO@SNG were depicted in Fig. 2c. A doublet can be found at 781.20/796.19 eV for Ru-CoO@SNG, along with a pair of satellite peaks at 786.71 and 801.70 eV, due to the $2p_{3/2}$ and $2p_{1/2}$ electrons of Co^{2+} [62–64], consistent with the formation of CoO in the samples, as evidenced in the above TEM measurements. CoO@SNG exhibited a similar feature with the peaks ca. +0.1 eV higher at 781.31 eV and 796.31 eV (Fig. 2c) [65]. This suggests effective electron transfer from Ru to Co in Ru-CoO@SNG, as compared to Ru@SNG and CoO@SNG, likely due to

the intimate contact between two components and the formation of heterojunctions, as manifested in TEM measurements (Fig. 1).

The N 1s and S 2p spectra are shown in Fig. S5c and S5d, where three N species can be resolved at 398.28 eV for pyridinic N, 399.68 eV for pyrrolic N, and 401.17 eV for graphitic N (Table S3) [66–68], whereas C—S—C can be identified at 163.82 eV [69,70], suggesting successful codoping of N and S into the carbon skeletons. In the O 1s spectra (Fig. S5e), the metal-O can be resolved at 530.04 eV in Ru-CoO@SNG, 529.94 eV in Ru@SNG, and 529.97 eV in CoO@SNG, consistent with the formation of CoO (as well as RuO₂).

3.2. Electrocatalytic activity

Remarkably, the Ru-CoO@SNG nanocomposites exhibited drastically enhanced electrocatalytic activity towards HER in alkaline media, as compared to SNG, Ru@SNG, and CoO@SNG. From the HER polarization curves in Fig. 3a, it can be seen that in N2-saturated 1 M KOH, the η_{10} of Ru-CoO@SNG was only -90 mV, markedly lower than -314 mV for Ru@SNG, whereas CoO@SNG and SNG could not reach a current density of 10 mA cm⁻² even at potentials significantly more negative than -0.4 V. This suggests that the Ru-CoO heterostructure played a dominant role in the HER activity, with minimum contributions from the SNG scaffold. The corresponding Tafel plots are shown in Fig. 3b where the Tafel slope was estimated to be 77 mV dec⁻¹ for Ru-CoO@SNG, which was much lower than those of Ru@SNG (145 mV dec⁻¹) and CoO@SNG (174 mV dec⁻¹), suggesting facile electron-transfer kinetics of HER on Ru-CoO@SNG. Such a performance is only somewhat subpar as compared to that of commercial Pt/C ($\eta_{10} = -60$ mV and Tafel slope 45 mV dec⁻¹). Consistent results were obtained in electrochemical impedance spectroscopy measurements. Fig. 3c presents the Nyquist plots at the overpotential of -87 mV in 1 M KOH. The Ru-CoO@SNG sample can be seen to display the lowest charge-transfer resistance (R_{ct}) of 4.5 Ω , in comparison to 832 Ω for Ru@SNG, 1790 Ω for CoO@SNG and 4340 Ω for SNG. The electrochemically active surface area (ECSA) of the nanocomposites was then quantitatively assessed and compared. Based on the cyclic voltammograms within the non-Faradaic region, the electrode double layer capacitance (Cdl) of Ru-CoO@SNG was quantified to be $3.34~\text{mF}~\text{cm}^{-2}$, much higher than those of Ru@SNG (2.74 mF $cm^{-2}),\ CoO@SNG\ (0.025\ mF\ cm^{-2})$ and SNG (0.025 mF $cm^{-2})$ (Fig. S6). This suggests that Ru-CoO@SNG possessed the largest ECSA that might facilitate the accessibility of the catalytic active sites.

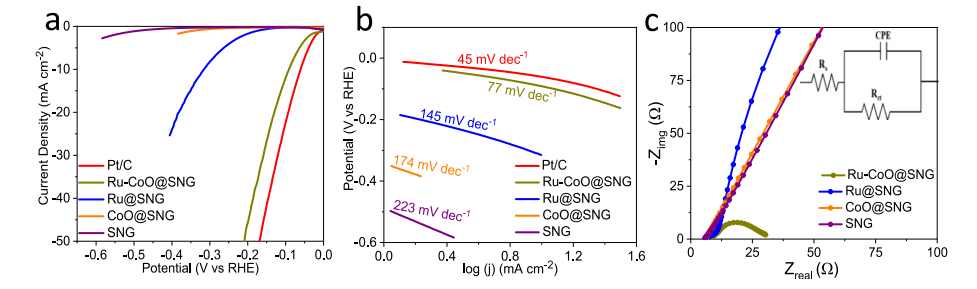


Fig. 3. (a) HER polarization curves of the series of nanocomposites and Pt/C in 1 M KOH at the rotation rate of 1600 rpm, potential sweep rate of 10 mV s⁻¹ and 85 % iR compensation. (b) The corresponding Tafel plots obtained from the polarization curves in (a). (c) Nyquist plots in 1 M KOH at the overpotential of -87 mV. Inset is the equivalent circuit, where R_s is the serial resistance, R_{ct} is the charge-transfer resistance, and CPE is the constant-phase element.

Notably, when the Ru-CoO@SNG nanocomposite was subject to acid leaching in 0.5 M H₂SO₄ for 24 h [71,72], the HER activity diminished dramatically, with η_{10} increased by 182 mV to $\,-\,272$ mV in 1 M KOH, which actually became close to that of Ru@SNG (-314 mV) (Fig. 4a). This demonstrates the significant role of cobalt oxide nanoparticles in dictating the electrocatalytic activity of the heterostructures towards HER, most likely due to effective Ru-Co charge transfer, where electron-deficient Ru was actually preferred for HER and heteroatom codoping facilitated the dispersion of the metal nanoparticles by altering their nucleation and growth kinetics, leading to a decrease of the nanoparticle size and increase of nanoparticle surface accessibility [73,74]. In fact, the performance is highly comparable to relevant catalysts reported recently in the literature (Table S4). Notably, the Ru-CoO@SNG nanocomposites were also active in acidic media, with $\eta_{10}\,$ = -95 mV, but markedly subpar as compared to Pt/C ($\eta_{10} = -22$ mV) (Fig. S7).

The nanocomposites also exhibited remarkable stability. Experimentally, after 1000 cycles within the potential window of -0.2 to +~0.2 V at the potential sweep rate of $10~\text{mV}~\text{s}^{-1}$ in 1~M KOH, the HER performance of Ru-CoO@SNG did not decay but was enhanced slightly with a 2 mV decrease of η_{10} and 20 mV of η_{80} , suggesting that the nanocomposites were actually activated for HER (Fig. 4b). In chronoamperometric tests at the overpotential of -153~mV in alkaline media, it can be seen from Fig. 4c that Ru-CoO@SNG retained the current density of 21 mA cm $^{-2}$ for ca. 2 h; by contrast, the current density decayed rather appreciably with commercial Pt/C.

4. Conclusion

In this study, nanocomposites of Ru-CoO heterostructured nanoparticle supported on N and S codoped graphene nanosheets were prepared by a facile pyrolytic procedure. The resultant Ru-CoO@SNG nanocomposites showed markedly enhanced electrocatalytic activity towards HER in 1 M KOH with a low η_{10} of only -90 mV, a Tafel slope

of 77 Mv dec⁻¹, as compared to the metal-free SNG, Ru@SNG and CoO@SNG, due to synergistic interactions between Ru and CoO nanoparticles where efficient charge transfer from Ru to Co occurred. Additional contributions might arise from the heteroatom doping within the graphene scaffold that facilitated the dispersion of the metal nanoparticles, accessibility of the catalytic active sites, and hence the electron-transfer kinetics. Results from this study highlight the significance of heterostructured nanoparticles in the development of high-performance electrocatalysts for electrochemical energy technologies.

CRediT authorship contribution statement

Warisha Naseeb: Data curation, Formal analysis, Writing – review & editing. Qiming Liu: Data curation, Formal analysis. Forrest Nichols: Data curation, Formal analysis. Dingjie Pan: Data curation, Formal analysis. Muhammad Kaleem Khosa: Funding acquisition, Formal analysis. Shaowei Chen: Conceptualization, Funding acquisition, Project administration, Resources, Writing – review & editing.

Data availability

Data will be made available on request.

Declaration of Competing Interest

The authors declare that they have no known competing financial interests or personal relationships that could have appeared to influence the work reported in this paper.

Acknowledgements

W.N. acknowledges the support by a research fellowship (IRSIP) from the Higher Education Commission, Pakistan. The work was supported, in part, by the National Science Foundation (CHE-1900235). TEM and XPS work were carried out at the National Center for Elec-

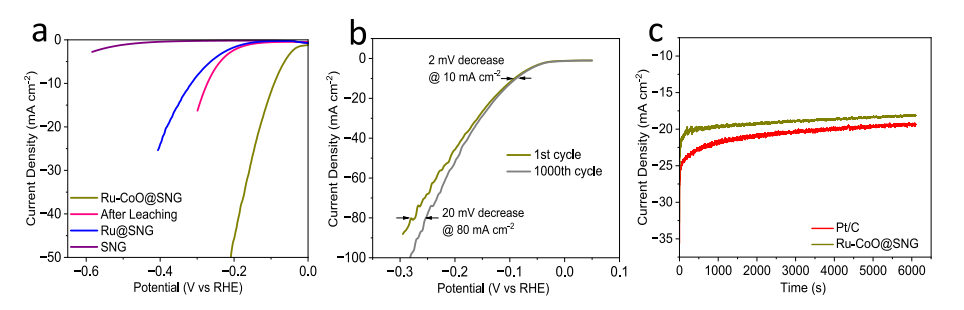


Fig. 4. (a) HER polarization curves of Ru-CoO@SNG in 1 M KOH before and after acid leaching treatment, in comparison to that of Ru@SNG. (b) HER polarization curves of Ru-CoO@SNG before and after 1000 CV cycles, and (c) i-t curves of Ru-CoO@SNG and Pt/C at the overpotential of -153 mV in 1 M KOH.

tron Microscopy and Molecular Foundry, Lawrence Berkeley National Laboratory, which is supported by the US Department of Energy, as part of a user project. We also thank Mr. J. Barnett for the assistance in XRD sample preparation and data acquisition and the X-ray Facility at University of California Santa Cruz for use of the Rigaku Smartlab Diffractometer, funded by the National Science Foundation (MRI-1126845).

Appendix A. Supplementary data

Supplementary data to this article can be found online at https://doi.org/10.1016/j.jelechem.2023.117272.

References

- [1] J. Zhang, J. Wu, X. Zou, K. Hackenberg, W. Zhou, W. Chen, J. Yuan, K. Keyshar, G. Gupta, A. Mohite, Discovering superior basal plane active two-dimensional catalysts for hydrogen evolution, Mater. Today 25 (2019) 28–34.
- [2] Q. Liu, J. Shen, X. Yu, X. Yang, W. Liu, J. Yang, H. Tang, H. Xu, H. Li, Y. Li, Unveiling the origin of boosted photocatalytic hydrogen evolution in simultaneously (S, P, O)-Codoped and exfoliated ultrathin g-C3N4 nanosheets, Appl. Catal. B: Environ. 248 (2019) 84–94.
- [3] K. Zhang, X. Liang, L. Wang, K. Sun, Y. Wang, Z. Xie, Q. Wu, X. Bai, M.S. Hamdy, H. Chen, Status and perspectives of key materials for PEM electrolyzer, Nano Res. Energy 1 (2022) e9120032.
- [4] Y. Qiu, Z. Liu, Q. Yang, X. Zhang, J. Liu, M. Liu, T. Bi, X. Ji, Atmospheric-temperature chain reaction towards ultrathin non-crystal-phase construction for highly efficient water splitting, Chem. Eur. J. 28 (2022) e202200683.
- [5] L. Zhang, J. Wang, P. Liu, J. Liang, Y. Luo, G. Cui, B. Tang, Q. Liu, X. Yan, H. Hao, M. Liu, R. Gao, X. Sun, Ni(OH)2 nanoparticles encapsulated in conductive nanowire array for high-performance alkaline seawater oxidation, Nano Res. 15 (2022) 6084–6090.
- [6] L. Zhang, J. Liang, L. Yue, K. Dong, J. Li, D. Zhao, Z. Li, S. Sun, Y. Luo, Q. Liu, G. Cui, A. Ali Alshehri, X. Guo, X. Sun, Benzoate anions-intercalated NiFe-layered double hydroxide nanosheet array with enhanced stability for electrochemical seawater oxidation, Nano Res. Energy 1 (2022) e9120028.
- [7] H.I. Karunadasa, C.J. Chang, J.R. Long, A molecular molybdenum-oxo catalyst for generating hydrogen from water. Nature 464 (2010) 1329–1333.
- [8] S. Deng, K. Zhang, D. Xie, Y. Zhang, Y. Zhang, Y. Wang, J. Wu, X. Wang, H.J. Fan, X. Xia, High-index-faceted Ni₃S₂ branch arrays as bifunctional electrocatalysts for efficient water splitting, Nano-Micro Lett. 11 (2019) 1–12.
- [9] Y. Li, J. Yin, L. An, M. Lu, K. Sun, Y.Q. Zhao, D. Gao, F. Cheng, P. Xi, FeS₂/CoS₂ interface nanosheets as efficient bifunctional electrocatalyst for overall water splitting, Small 14 (2018) 1801070.
- [10] X. Fang, X. Wang, L. Ouyang, L. Zhang, S. Sun, Y. Liang, Y. Luo, D. Zheng, T. Kang, Q. Liu, Amorphous Co-Mo-B Film: A High-Active Electrocatalyst for Hydrogen Generation in Alkaline Seawater, Molecules 27 (2022) 7617.
- [11] A. Eftekhari, Electrocatalysts for hydrogen evolution reaction, Int. J. Hydrogen Energy 42 (2017) 11053–11077.
- [12] H. Yu, J. Xu, D. Gao, J. Fan, J. Yu, Triethanolamine-mediated photodeposition formation of amorphous Ni-P alloy for improved H₂-evolution activity of g-C₃N₄, Sci. Chin. Mater. 63 (2020) 2215–2227.
- [13] X. Zou, Y. Zhang, Noble metal-free hydrogen evolution catalysts for water splitting, Chem. Soc. Rev. 44 (2015) 5148–5180.
- [14] W.H. Lai, L.F. Zhang, W.B. Hua, S. Indris, Z.C. Yan, Z. Hu, B. Zhang, Y. Liu, L. Wang, M. Liu, General π-electron-assisted strategy for Ir, Pt, Ru, Pd, Fe, Ni single-atom electrocatalysts with bifunctional active sites for highly efficient water splitting, Angew. Chem. Int. Ed. 58 (2019) 11868–11873.
- [15] L. Ouyang, X. He, Y. Sun, L. Zhang, D. Zhao, S. Sun, Y. Luo, D. Zheng, A.M. Asiri, Q. Liu, J. Zhao, X. Sun, RuO₂ nanoparticle-decorated TiO2 nanobelt array as a highly efficient electrocatalyst for the hydrogen evolution reaction at all pH values, Inorg. Chem. Front. 9 (2022) 6602–6607.
- [16] M. Liu, C. Zhang, W. Chen, Novel nanomaterials as electrocatalysts for fuel cells, Nanomaterials for Green Energy, Elsevier 2018, pp. 169-204.
- [17] M. Dai, D. Zhao, H. Liu, Y. Tong, P. Hu, X. Wu, Nanostructure and doping engineering of ZnCoP for high performance electrolysis of water, Mater. Today Energy 16 (2020) 100412.
- [18] W.-J. Jiang, T. Tang, Y. Zhang, J.-S. Hu, Synergistic modulation of non-preciousmetal electrocatalysts for advanced water splitting, Acc. Chem. Res. 53 (2020) 1111–1123.
- [19] H. Coskun, A. Aljabour, P. de Luna, H. Sun, N. Nishiumi, T. Yoshida, G. Koller, M. G. Ramsey, T. Greunz, D. Stifter, Metal-free hydrogen-bonded polymers mimic noble metal electrocatalysts, Adv. Mater. 32 (2020) 1902177.
- [20] L. Hui, Y. Xue, Y. Liu, Y. Li, Efficient hydrogen evolution on nanoscale graphdiyne, Small 17 (2021) 2006136.
- [21] D. Wang, Q. Li, C. Han, Q. Lu, Z. Xing, X. Yang, Atomic and electronic modulation of self-supported nickel-vanadium layered double hydroxide to accelerate water splitting kinetics, Nat. Commun. 10 (2019) 1–12.
- [22] S.-Y. Bae, J. Mahmood, I.-Y. Jeon, J.-B. Baek, Recent advances in ruthenium-based electrocatalysts for the hydrogen evolution reaction, Nanoscale Horiz. 5 (2020) 43–56.

- [23] C.C. McCrory, S. Jung, I.M. Ferrer, S.M. Chatman, J.C. Peters, T.F. Jaramillo, Benchmarking hydrogen evolving reaction and oxygen evolving reaction electrocatalysts for solar water splitting devices, J. Am. Chem. Soc. 137 (2015) 4347–4357.
- [24] J. Yu, Q. He, G. Yang, W. Zhou, Z. Shao, M. Ni, Recent advances and prospective in ruthenium-based materials for electrochemical water splitting, Acs Catal. 9 (2019) 9973–10011
- [25] J. Creus, J. De Tovar, N. Romero, J. García-Antón, K. Philippot, R. Bofill, X. Sala, Ruthenium nanoparticles for catalytic water splitting, ChemSusChem 12 (2019) 2493–2514.
- [26] C.-T. Dinh, A. Jain, F.P.G. de Arquer, P. De Luna, J. Li, N. Wang, X. Zheng, J. Cai, B. Z. Gregory, O. Voznyy, Multi-site electrocatalysts for hydrogen evolution in neutral media by destabilization of water molecules, Nature Energy 4 (2019) 107–114.
- [27] L. Yu, Q. Zhu, S. Song, B. McElhenny, D. Wang, C. Wu, Z. Qin, J. Bao, Y. Yu, S. Chen, Non-noble metal-nitride based electrocatalysts for high-performance alkaline seawater electrolysis, Nat. Commun. 10 (2019) 1–10.
- [28] P. Zhai, Y. Zhang, Y. Wu, J. Gao, B. Zhang, S. Cao, Y. Zhang, Z. Li, L. Sun, J. Hou, Engineering active sites on hierarchical transition bimetal oxides/sulfides heterostructure array enabling robust overall water splitting, Nat. Commun. 11 (2020) 1–12.
- [29] X. Wang, C. Xu, M. Jaroniec, Y. Zheng, S.-Z. Qiao, Anomalous hydrogen evolution behavior in high-pH environment induced by locally generated hydronium ions, Nat. Commun. 10 (2019) 1–8.
- [30] B. Lu, L. Guo, F. Wu, Y. Peng, J.E. Lu, T.J. Smart, N. Wang, Y.Z. Finfrock, D. Morris, P. Zhang, Ruthenium atomically dispersed in carbon outperforms platinum toward hydrogen evolution in alkaline media, Nat. Commun. 10 (2019) 1–11.
- [31] J. Liu, Y. Zheng, D. Zhu, A. Vasileff, T. Ling, S.-Z. Qiao, Identification of pH-dependent synergy on Ru/MoS 2 interface: a comparison of alkaline and acidic hydrogen evolution, Nanoscale 9 (2017) 16616–16621.
- [32] J. Chen, L. Zhang, J. Li, X. He, Y. Zheng, S. Sun, X. Fang, D. Zheng, Y. Luo, Y. Wang, J. Zhang, L. Xie, Z. Cai, Y. Sun, A.A. Alshehri, Q. Kong, C. Tang, X. Sun, Highefficiency overall alkaline seawater splitting: using a nickel-iron sulfden anosheet array as a bifunctional electrocatalyst, J. Mater. Chem. A 11 (2023) 1116–1122.
- [33] J. Zhang, L. Yu, Y. Chen, X.F. Lu, S. Gao, X.W. Lou, Designed formation of double-shelled Ni–Fe layered-double-hydroxide nanocages for efficient oxygen evolution reaction, Adv. Mater. 32 (2020) 1906432.
- [34] H. Han, Y. Qiu, H. Zhang, T. Bi, Q. Yang, M. Liu, J. Zhou, X. Ji, Lattice-disorder layer generation from liquid processing at room temperature with boosted nanointerface exposure toward water splitting, Sustain. Energy Fuels 6 (2022) 3008–3013.
- [35] Q. He, D. Tian, H. Jiang, D. Cao, S. Wei, D. Liu, P. Song, Y. Lin, L. Song, Achieving efficient alkaline hydrogen evolution reaction over a Ni_5P_4 catalyst incorporating single-atomic Ru sites, Adv. Mater. 32 (2020) 1906972.
- [36] N. Yao, P. Li, Z. Zhou, Y. Zhao, G. Cheng, S. Chen, W. Luo, Synergistically tuning water and hydrogen binding abilities over Co4N by Cr doping for exceptional alkaline hydrogen evolution electrocatalysis, Adv. Energy Mater. 9 (2019) 1902449.
- [37] Q. Liu, S. Sun, L. Zhang, Y. Luo, Q. Yang, K. Dong, X. Fang, D. Zheng, A.A. Alshehri, X. Sun, N, O-doped carbon foam as metal-free electrocatalyst for efficient hydrogen production from seawater, Nano Res. 15 (2022) 8922–8927.
- [38] F. Gao, J. He, H. Wang, J. Lin, R. Chen, K. Yi, F. Huang, Z. Lin, M. Wang, Temediated electro-driven oxygen evolution reaction, Nano Res. Energy 1 (2022) e9120029.
- [39] M.K. Diallo, Recent advances on heteroatom (N, B) doped carbons based hybrid catalysts for diverse applications, SSRN 4123411, (2022).
- [40] X. Gao, J. Chen, X. Sun, B. Wu, B. Li, Z. Ning, J. Li, N. Wang, Ru/RuO₂ nanoparticle composites with N-doped reduced graphene oxide as electrocatalysts for hydrogen and oxygen evolution, ACS Appl. Nano Mater. 3 (2020) 12269–12277.
- [41] X. Jiang, H. Jang, S. Liu, Z. Li, M.G. Kim, C. Li, Q. Qin, X. Liu, J. Cho, The heterostructure of Ru₂P/WO₃/NPC synergistically promotes H₂O dissociation for improved hydrogen evolution, Angew. Chem. 133 (2021) 4156–4162.
- [42] T. Liu, A. Li, C. Wang, W. Zhou, S. Liu, L. Guo, Interfacial electron transfer of Ni₂P-NiP₂ polymorphs inducing enhanced electrochemical properties, Adv. Mater. 30 (2018) 1803590.
- [43] Y. Liu, S. Liu, Y. Wang, Q. Zhang, L. Gu, S. Zhao, D. Xu, Y. Li, J. Bao, Z. Dai, Ru modulation effects in the synthesis of unique rod-like Ni@Ni₂P-Ru heterostructures and their remarkable electrocatalytic hydrogen evolution performance, J. Am. Chem. Soc. 140 (2018) 2731–2734.
- [44] H. Wang, X. Cheng, Y. Tong, Coupling of ruthenium with hybrid metal nitrides heterostructure as bifunctional electrocatalyst for water electrolysis, J. Colloid Interface Sci. 629 (2023) 155–164.
- [45] D.T. Tran, S. Prabhakaran, D.H. Kim, N. Hameed, H. Wang, N.H. Kim, J.H. Lee, Ruthenium single atoms implanted continuous MoS₂-Mo₂C heterostructure for high-performance and stable water splitting, Nano Energy 88 (2021) 106277.
- [46] H. Sun, J.-M. Yang, J.-G. Li, Z. Li, X. Ao, Y.-Z. Liu, Y. Zhang, Y. Li, C. Wang, J. Tang, Synergistic coupling of NiTe nanoarrays with RuO₂ and NiFe-LDH layers for highefficiency electrochemical-/photovoltage-driven overall water splitting, Appl. Catal. B: Environ. 272 (2020) 118988.
- [47] B. Geng, F. Yan, L. Liu, C. Zhu, B. Li, Y. Chen, Ni/MoC heteronanoparticles encapsulated within nitrogen-doped carbon nanotube arrays as highly efficient self-supported electrodes for overall water splitting, Chem. Eng. J. 406 (2021) 126815.
- [48] D.J. Pan, W.M. Liu, F. Nichols, R. Mercado, H.-L. Kuo, J.Q. Lu, F. Bridges, S.W. Chen, Impacts of ruthenium valence state on the electrocatalytic activity of ruthenium ion-complexed graphitic carbon nitride/reduced graphene oxide

- nanosheets towards hydrogen evolution reaction, J. Colloid Interface Sci. 629 (2023) 591-597.
- [49] F. Bao, Z. Yang, Y. Yuan, P. Yu, G. Zeng, Y. Cheng, Y. Lu, J. Zhang, H. Huang, Synergistic cascade hydrogen evolution boosting via integrating surface oxophilicity modification with carbon layer confinement, Adv. Funct. Mater. 32 (2022) 2108991.
- [50] K. Deori, S. Deka, Morphology oriented surfactant dependent CoO and reaction time dependent Co₃O₄ nanocrystals from single synthesis method and their optical and magnetic properties, CrystEngComm 15 (2013) 8465–8474.
- [51] M. Sharma, J.-H. Jang, D.Y. Shin, J.A. Kwon, D.-H. Lim, D. Choi, H. Sung, J. Jang, S.-Y. Lee, K.Y. Lee, Work function-tailored graphene via transition metal encapsulation as a highly active and durable catalyst for the oxygen reduction reaction. Energy Environ. Sci. 12 (2019) 2200–2211.
- [52] C. Jung, T. Zhao, L. Zeng, P. Tan, Vertically aligned carbon nanotube-ruthenium dioxide core-shell cathode for non-aqueous lithium-oxygen batteries, J. Power Sources 331 (2016) 82–90.
- [53] J. Lv, Z. Rong, L. Sun, C. Liu, A.-H. Lu, Y. Wang, J. Qu, Catalytic conversion of biomass-derived levulinic acid into alcohols over nanoporous Ru catalyst, Catal, Sci. Technol. 8 (2018) 975–979.
- [54] T. He, Y. Peng, Q. Li, J.E. Lu, Q. Liu, R. Mercado, Y. Chen, F. Nichols, Y. Zhang, S. Chen, Nanocomposites based on ruthenium nanoparticles supported on cobalt and nitrogen-codoped graphene nanosheets as bifunctional catalysts for electrochemical water splitting, ACS Appl. Mater. Interfaces 11 (2019) 46912–46919.
- [55] W. Chen, C. Hao, Z. Qiu, X. Zhang, H. Xu, B. Yu, S. Chen, High-energy-density asymmetric supercapacitor based on free-standing Ti₃C₂T_x@NiO-reduced graphene oxide heterostructured anode and defective reduced graphene oxide hydrogel cathode, ACS Appl. Mater. Interfaces 14 (2022) 19534–19546.
- [56] K. Dave, K.H. Park, M. Dhayal, Two-step process for programmable removal of oxygen functionalities of graphene oxide: functional, structural and electrical characteristics, RSC Adv. 5 (2015) 95657–95665.
- [57] Y. Yan, J. Huang, X. Wang, T. Gao, Y. Zhang, T. Yao, B. Song, Ruthenium incorporated cobalt phosphide nanocubes derived from a prussian blue analog for enhanced hydrogen evolution, Front. Chem. 6 (2018) 521.
- [58] B.M. Stühmeier, R.J. Schuster, L. Hartmann, S. Selve, H.A. El-Sayed, H.A. Gasteiger, Modification of the Electrochemical Surface Oxide Formation and the Hydrogen Oxidation Activity of Ruthenium by Strong Metal Support Interactions, J. Electrochem. Soc. 169 (2022) 034519.
- [59] Q. Liu, B. Lu, F. Nichols, J. Ko, R. Mercado, F. Bridges, S. Chen, Rapid preparation of carbon-supported ruthenium nanoparticles by magnetic induction heating for efficient hydrogen evolution reaction in both acidic and alkaline media, SusMat 2 (2022) 335–346.
- [60] J. Wang, Q. Yu, H. Li, R. Li, S. Zeng, Q. Yao, Z. Guo, H. Chen, K. Qu, Natural DNAassisted RuP₂ on highly graphitic N, P-codoped carbon for pH-wide hydrogen evolution, Chem. Commun. 57 (2021) 7284–7287.

- [61] N. Wang, S. Ning, X. Yu, D. Chen, Z. Li, J. Xu, H. Meng, D. Zhao, L. Li, Q. Liu, Graphene composites with Ru-RuO₂ heterostructures: Highly efficient Mott–Schottky-type electrocatalysts for pH-universal water splitting and flexible zinc-air batteries, Appl. Catal. B: Environ. 302 (2022) 120838.
- [62] Y. Song, T. He, Y. Zhang, C. Yin, Y. Chen, Q. Liu, Y. Zhang, S. Chen, Cobalt single atom sites in carbon aerogels for ultrasensitive enzyme-free electrochemical detection of glucose. J. Electroanal. Chem. 906 (2022) 116024.
- [63] Q. Liu, S. McNair, F. Nichols, B. Lu, B. Yu, D. Pan, J. Ko, A. Bhuller, F. Bridges, S. Chen, Ultrafast synthesis of cobalt/carbon nanocomposites by magnetic induction heating for oxygen evolution reaction, Adv. Sens. Energy Mater. (2023) 100046.
- [64] M.S. Ahmed, B. Choi, Y.-B. Kim, Development of highly active bifunctional electrocatalyst using Co₃O₄ on carbon nanotubes for oxygen reduction and oxygen evolution, Sci. Rep. 8 (2018) 1–10.
- [65] J.X. Flores-Lasluisa, J. Quílez-Bermejo, A.C. Ramírez-Pérez, F. Huerta, D. Cazorla-Amorós, E. Morallón, Copper-doped cobalt spinel electrocatalysts supported on activated carbon for hydrogen evolution reaction, Materials 12 (2019) 1302.
- [66] P. Chu, Y. Zhang, J. He, J. Chen, J. Zhuang, Y. Li, X. Ren, P. Zhang, L. Sun, B. Yu, Defective Fe₃O_{4-x} few-atom clusters anchored on nitrogen-doped carbon as efficient oxygen reduction electrocatalysts for high-performance zinc-air batteries, Small Methods 6 (2022) 2200207.
- [67] X. Wu, Y. Sun, T. He, Y. Zhang, G.-J. Zhang, Q. Liu, S. Chen, Iron, nitrogen-doped carbon aerogels for fluorescent and electrochemical dual-mode detection of glucose, Langmuir 37 (2021) 11309–11315.
- [68] F. Nichols, J.E. Lu, R. Mercado, M.D. Rojas-Andrade, S. Ning, Z. Azhar, J. Sandhu, R. Cazares, C. Saltikov, S. Chen, Antibacterial activity of nitrogen-doped carbon dots enhanced by atomic dispersion of copper, Langmuir 36 (2020) 11629–11636.
- [69] S. Chen, Y. Yan, P. Hao, M. Li, J. Liang, J. Guo, Y. Zhang, S. Chen, W. Ding, X. Guo, Iron nanoparticles encapsulated in S, N-codoped carbon: Sulfur doping enriches surface electron density and enhances electrocatalytic activity toward oxygen reduction, ACS Appl. Mater. Interfaces 12 (2020) 12686–12695.
- [70] D. Zhao, L. Li, L. Xie, N. Zhou, S. Chen, Sulfur codoping enables efficient oxygen electroreduction on FeCo alloy encapsulated in N-Doped carbon nanotubes, J. Alloys Compd. 741 (2018) 368–376.
- [71] I. Boukerche, N. Habbache, N. Alane, S. Djerad, L. Tifouti, Dissolution of cobalt from CoO/Al₂O₃ catalyst with mineral acids, Ind. Eng. Chem. Res. 49 (2010) 6514–6520.
- [72] P. Mwamba, J.H. Masinja, J. Manchisi, L. Kabondo, Sulphuric acid bake-leach process for the treatment of mixed copper-cobalt oxide ores, J. Miner. Mater. Charact. Eng. 10 (2022) 174–184.
- [73] M. Sahoo, S. Ramaprabhu, Nitrogen and sulfur co-doped porous carbon is an efficient electrocatalyst as platinum or a hoax for oxygen reduction reaction in acidic environment PEM fuel cell?, Energy 119 (2017) 1075–1083
- [74] X. Li, G. Liu, H. Zheng, K. Sun, L. Wan, J. Cao, S. Asif, Y. Cao, W. Si, F. Wang, Recent advances on heteroatom-doped porous carbon—based electrocatalysts for oxygen reduction reaction, Energies 16 (2022) 128.